Fast technetium-99m liver SPECT for evaluation of the pretreatment procedure for radioembolization dosimetry

Sandra van der Velden[a)] and Martijn M. A. Dietze
Radiology and Nuclear Medicine, University Medical Center Utrecht, P.O. Box 85500, 3508 GA, Utrecht, Netherlands
Image Sciences Institute, Utrecht University and University Medical Center Utrecht, P.O. Box 85500, 3508 GA, Utrecht, Netherlands

Max A. Viergever
Image Sciences Institute, Utrecht University and University Medical Center Utrecht, P.O. Box 85500, 3508 GA, Utrecht, Netherlands

Hugo W. A. M. de Jong
Radiology and Nuclear Medicine, University Medical Center Utrecht, P.O. Box 85500, 3508 GA, Utrecht, Netherlands

(Received 11 June 2018; revised 15 October 2018; accepted for publication 16 October 2018; published 13 November 2018)

Purpose: The efficiency of radioembolization procedures could be greatly enhanced if results of the ^{99m}Tc-MAA pretreatment procedure were immediately available in the interventional suite, enabling 1-day procedures as a result of direct estimation of the hepatic radiation dose and lung shunt fraction. This would, however, require a relatively fast, but still quantitative, SPECT procedure, which might be achieved with acquisition protocols using nonuniform durations of the projection images.
Methods: SPECT liver images of the 150-MBq ^{99m}Tc-MAA pretreatment procedure were simulated for eight different lesion locations and two different lesion sizes using the digital XCAT phantom for both single- and dual-head scanning geometries with respective total acquisition times of 1, 2, 5, 10, and 30 min. Three nonuniform projection-time acquisition protocols ("half-circle SPECT (HCS)," "nonuniform SPECT (NUS) I," and "NUS II") for fast quantitative SPECT of the liver were designed and compared with the standard uniform projection-time protocol. Images were evaluated in terms of contrast-to-noise ratio (CNR), activity recovery coefficient (ARC), tumor/non-tumor (T/N) activity concentration ratio, and lung shunt fraction (LSF) estimation. In addition, image quality was verified with a physical phantom experiment, reconstructed with both clinical and Monte Carlo-based reconstruction software.
Results: Simulations showed no substantial change in image quality and dosimetry by usage of a nonuniform projection-time acquisition protocol. Upon shortening acquisition times, CNR dropped, but ARC, T/N ratio, and LSF estimates were stable across all simulated acquisition times. Results of the physical phantom were in agreement with those of the simulations.
Conclusion: Both uniform and nonuniform projection-time acquisition liver SPECT protocols yield accurate dosimetric metrics for radioembolization treatment planning in the interventional suite within 10 min, without compromising image quality. Consequently, fast quantitative SPECT of the liver in the interventional suite is feasible. © *2018 The Authors. Medical Physics published by Wiley Periodicals, Inc. on behalf of American Association of Physicists in Medicine.* [https://doi.org/10.1002/mp.13253]

Key words: acquisition protocol, interventional imaging, nuclear imaging, radioembolization, SPECT

1. INTRODUCTION

Yttrium-90 (^{90}Y) radioembolization is a treatment for unresectable liver malignancies in which radioactive microspheres are injected into the hepatic artery.[1–3] Prior to the treatment, 150 MBq technetium-99m-macroaggregated albumin (^{99m}Tc-MAA) is given as a simulation of the deposition of the microspheres.[2] The distribution of the administered activity is assessed on planar scintigraphy and/or a single-photon emission computed tomography (SPECT)/computed tomography (CT) scan, and is used to evaluate the lung shunt fraction (LSF) and the presence of extrahepatic depositions, and to calculate the optimal ^{90}Y dosage based on the partition model.[3,4]

Currently, the ^{99m}Tc-MAA activity is given during a procedure preceding the actual treatment, sometimes separated by 2 or 3 weeks,[2] due to the need to image the patient at the nuclear medicine department for assessment of the ^{99m}Tc-MAA distribution. Having nuclear imaging directly available in the interventional suite would therefore have several advantages. Most importantly, this would simplify implementing radioembolization as a 1-day procedure,[5,6] shortening procedure times significantly and potentially making such a fast procedure widely available. In addition, the prognostic power of the pretreatment procedure may be greatly enhanced by having the catheter in the exact same position as for the treatment.[7] Furthermore, the physician will be provided with direct dose feedback, allowing for real-time adjustments if necessary.

Availability of nuclear images in the interventional suite can be achieved by installation of a SPECT/CT scanner in

© 2018 The Authors. Medical Physics published by Wiley Periodicals, Inc. on behalf of American Association of Physicists in Medicine. This is an open access article under the terms of the Creative Commons Attribution-NonCommercial-NoDerivs License, which permits use and distribution in any medium, provided the original work is properly cited, the use is non-commercial and no modifications or adaptations are made.

the interventional suite. As an alternative, one could use a mobile or handheld gamma camera.[8,9] Also, worth mentioning in this context is a mobile hybrid imaging device, combining a conventional c-arm with gamma cameras, which is currently being developed by our group.[10,11] It has been shown that this hybrid imaging device could safely replace current planar imaging in the nuclear medicine department for the estimation of lung shunt fraction,[12] giving acceptable estimates within 10 s. However, assessment of LSF on SPECT/CT images is more accurate than estimations based on planar scintigraphy images.[13] In addition, SPECT/CT images are needed for treatment planning using the partition model.[3,4]

To make a 1-day procedure attractive for usage in routine clinical practice, acquisition of a SPECT/CT scan should ideally not take more than 10 min (current clinical practice: 30 min), which is comparable with the scan and preparation time needed for a cone-beam CT. In addition, reducing the acquisition time to 10 min would help avoiding clot forming in the catheter and maintaining sterility. However, reducing acquisition times will reduce image quality owing to increased noise and might compromise quantitative accuracy, which is important for radioembolization dosimetry and treatment planning.

SPECT image quality may be improved by using nonuniform projection-time acquisition protocols, in which more time is spent at angles where the count rate is high.[14–17] Usage of nonuniform acquisition time protocols might therefore counteract the loss of image quality due to reduced total acquisition times. One of the simplest nonuniform projection-time acquisition protocols is a half-circle SPECT protocol as is clinically used in cardiac scanning. The rationale of this approach is that the heart is located in the left anterior aspect of the thorax. Consequently, photons coming from the left anterior aspect of the thorax are significantly attenuated when imaged from the back of the patient and might not contribute to image quality. Similar reasoning can be applied to liver SPECT. The liver is located at the right side of the body. Therefore, radiation emitted from the left side of the body is markedly attenuated, contributing less to image quality. For equal total acquisition times, more counts are obtained for a right anterior 180° orbit than for a 360° orbit. For the appropriate activity distributions, such half-circle SPECT acquisitions can generally yield reasonable reconstructed images. More complex acquisition time protocols than half-circle SPECT that are tailored to the expected activity distribution[14–17] might counteract the loss of image quality by the reduced acquisition times to an even larger extent.

The goal of this paper was to investigate the feasibility of acquiring fast liver SPECT scans without compromising the evaluation of the pretreatment procedure for radioembolization dosimetry and treatment planning. In addition, the potential benefit of three nonuniform projection-time acquisition protocols was evaluated.

2. MATERIALS AND METHODS

2.A. Acquisition protocols

Impact of shortening acquisition time on image quality was evaluated by simulating 150-MBq technetium-99m (^{99m}Tc) SPECT images acquired with a total acquisition time of 1, 2, 5, and 10 min, respectively, for a single-head system and for a dual-head system with the cameras in a 90-degree configuration, respectively. These images were compared with reference images obtained by simulating the current clinical protocol of a dual-head system with a total scan time of 30 min.

Spending more time at angles where the count rate is high has been shown to improve image quality. [14–17] Therefore, three nonuniform projection-time protocols, half-circle SPECT (HCS), nonuniform SPECT (NUS) I, and NUS II, were designed and compared with the standard uniform projection-time protocol in which all projections are acquired with equal acquisition times (Fig. 1, first column). In the nonuniform projection-time protocols, the total acquisition time was kept equal to the uniform projection-time protocol, only the distribution of the total time over the views was changed.

The half-circle SPECT protocol was based on clinically used dedicated cardiac scanners, in which a 180-degree rotation is standard. In this protocol, the 180-degree arc closest to the volume-of-interest (VOI) is scanned (Fig. 1, second column).

In the NUS protocol (Fig. 1, third column), a 360-degree arc is scanned, but with a nonuniform view time distribution. The 360-degree arc is divided into two parts, where 3/4th of the total acquisition time is spent at the 180-degree arc scanned with the HCS protocol and 1/4th of the total acquisition time at the other 180 degrees. We will refer to this protocol as NUS I.

A single-head system is more flexible than a dual-head system with respect to acquisition time distributions. Therefore, a second NUS protocol was designed (NUS II), which can only be executed with a single-head SPECT system (Fig. 1, fourth column). In this protocol, the 360-degree arc is divided into four parts of 90 degrees each. Half of the total acquisition time is spent at the 90-degree arc closest to the VOI, 7/32th of the total time is spent at each of the two adjacent 90-degree arcs and 1/16th of the time is spent at the opposite 90-degree arc.

For all acquisition protocols and total acquisition times, the view times per angle are indicated in Table I.

2.B. Simulation of SPECT images

2.B.1. Phantom

The digital four-dimensional extended cardiac-torso (XCAT) phantom[18] was used to provide a realistic anthropomorphic model suitable for SPECT simulations. All simulations were performed with a normal weight male (BMI: 25.8 kg/m^2) phantom without breathing motion. To

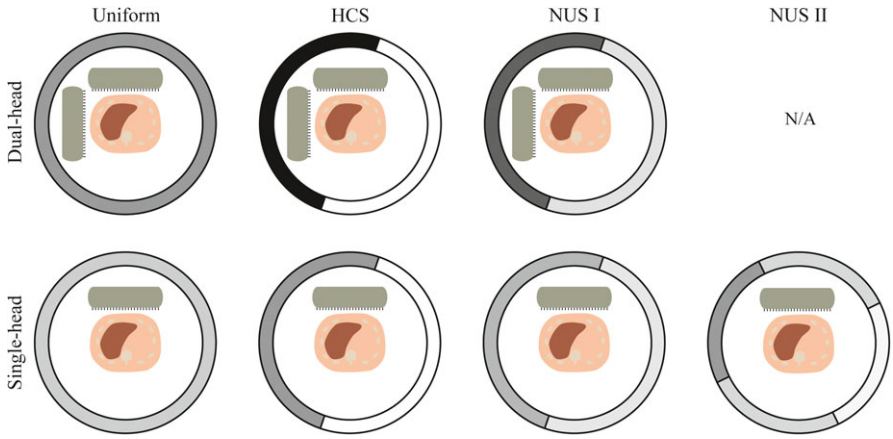

FIG. 1. Schematic overview of evaluated acquisition protocols for fast liver SPECT. The gray-scale ring indicates the acquisition time distribution: a darker color means more time is spent at that angle (exact times can be found in Table I). Upper row: dual-head system, lower row: single-head system. Column 1: uniform projection-time distribution; column 2: half-circle SPECT (HCS); column 3: nonuniform SPECT I (NUS I); column 4: nonuniform SPECT II (NUS II). [Color figure can be viewed at wileyonlinelibrary.com]

TABLE I. View time per angle [s/view] for the different time windows (indicated in gray in Fig. 1) for all acquisition protocols and total acquisition times, given a 360-degree acquisition and 120 projections. For example, 2 – 0 with the dual-head HCS protocol and 1 min total acquisition time means 2 s is spent at each view in the first 180-degree arc and 0 s is spent at each view in the second 180-degree arc.

	Dual-head			Single-head			
Total acquisition time (min)	Uniform	HCS	NUS I	Uniform	HCS	NUS I	NUS II
1	1	2 – 0	1.5 – 0.5	0.5	1 – 0	0.75 – 0.25	1 – 0.44 – 0.13
2	2	4 – 0	3 – 1	1	4 – 0	1.5 – 0.5	2 – 0.88 – 0.25
5	5	10 – 0	7.5 – 2.5	2.5	5 – 0	3.25 – 1.25	5 – 2.19 – 0.63
10	10	20 – 0	15 – 5	5	10 – 0	7.5 – 2.5	10 – 4.38 – 1.25
30	30	60 – 0	45 – 15	–	–	–	–

investigate the influence of lesion size and location on image quality obtained with the different protocols and acquisition times, lesions of 10 and 20 mm in diameter were positioned in each of the eight liver segments (Fig. 2). To avoid scatter counts from nontarget lesions into the target lesion, 16 different phantom configurations were generated based on lesion size and position. A total activity of 150-MBq ^{99m}Tc was simulated, which is the standard amount of ^{99m}Tc administered to radioembolization patients during the pretreatment procedure.[1] A realistic radioembolization patient was simulated by setting the tumor/non-tumor (T/N) activity concentration ratio to 8 and assuming a lung shunt fraction of 5%.[19.]

2.B.2. Simulations

A total of 120 projections acquired with a low-energy high-resolution (LEHR) parallel hole collimator were simulated with the Utrecht Monte Carlo System (UMCS), including scatter and attenuation.[20,21] The energy window was set to 140 keV ± 7.5%. Depth-dependent collimator response was modeled with kernels based on a Monte Carlo radiation transport code (MCNPX) model[22] of a Symbia T SPECT/CT system (Siemens Healthcare, Erlangen, Germany).[21,23] Projections were simulated on a matrix of 128 × 128 pixels,

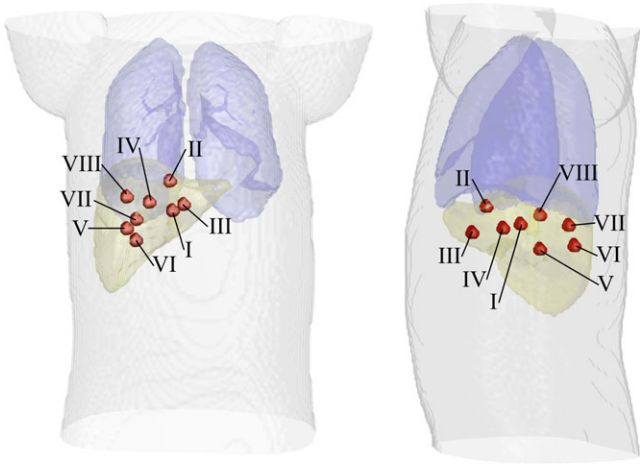

FIG. 2. Rendering of the phantom (anterior and right lateral view) used in the simulations, with the lungs in blue and the liver in yellow. The red dots indicate the locations of the lesions in the different lesion segments. Note that in each phantom realization, only one lesion was positioned in the liver. [Color figure can be viewed at wileyonlinelibrary.com]

with a pixel size of 4.8 × 4.8 mm^2. For each combination of phantom, protocol, scan geometry (single- or dual-head), and total acquisition time (Table II), 25 projection measurements were created by adding Poisson noise, scaled by the time per

TABLE 2. Overview of parameters. Each combination of parameters was simulated, except the nonuniform SPECT II protocol (single-head only) and 30-min acquisition time (dual-head only). This yielded a total number of 496 combinations for which 25 different noise realizations were simulated. Parameter values in bold indicate reference values. All phantoms had an LSF of 5% and a T/N ratio of 8:1.

Acquisition parameters	Scan geometry	Protocol		Total acquisition time (min)
	Single-head	**Uniform**		1
	Dual-head	Half-circle SPECT		2
		Non-uniform SPECT I		5
		Non-uniform SPECT II		10
				30
Phantom parameters	Lesion size	Lesion location		
	10 mm diameter	I	V	
	20 mm diameter	II	VI	
		III	VII	
		IV	**VIII**	

projection and the total activity, to the simulated noise-free projections.

UMCS was used to reconstruct the simulated projections into a volume of 128 × 128 × 128 voxels with a voxel size of 4.8 × 4.8 × 4.8 mm^3 using an ordered subset expectation-maximization (OSEM) algorithm with 10 iterations and 8 subsets, including attenuation and Monte Carlo scatter correction and depth-dependent resolution recovery.[20,21] To reconstruct projections of nonuniform projection-time protocols, viewing time per angle was incorporated into the reconstruction as follows:

$$f_i^{k+1} = \frac{f_i^k}{\sum_j t_j} \cdot \frac{1}{\sum_j p_{i,j} \cdot n_j} \cdot \sum_j \left[p_{i,j} \cdot \frac{s_j}{\sum_i p_{i,j} \cdot f_i^k \cdot t_j} \right]. \quad (1)$$

Here, f_i^k is the k^{th} estimate of the activity distribution at voxel i, s_j is the measured projection at angle j, $P = \{p_{i,j}\}$ is the system matrix, t_j is the duration of the projection-image acquisition at angle j, and

$$n_j = \begin{cases} 1, & t_j \neq 0 \\ 0, & t_j = 0 \end{cases}.$$

The factor n_j ensures the normalization map complies with the number of angles imaged. Since system sensitivity was incorporated in the depth-dependent collimator response of the forward projector, this resulted in quantitative reconstructions with voxel values representing activity concentration in Bq/voxel.

2.C. Image quality metrics

To compare the different protocols and acquisition times, image quality was evaluated in terms of contrast-to-noise ratio (CNR). In addition, the following dosimetry-related metrics were calculated: the activity recovery coefficient (ARC), the tumor/non-tumor (T/N) ratio, and estimated LSF. Accurate determination of these metrics is a first step toward the calculation of absorbed doses in gray. For all metrics, the mean and standard deviation over the 25 simulated noise realizations were reported.

For all metrics except lung shunt fraction, a lesion VOI and a background VOI are needed. These VOIs were created using the activity map of the XCAT phantom. Lesion VOIs were defined as all lesion voxels of the phantom. The background VOI was defined as all liver voxels of the phantom, excluding the lesion voxels. For each combination of lesion position and size, a specific background VOI was generated. To exclude voxels affected by collimator blurring and partial volume effects, the background VOI was eroded by 1 cm.

For the calculation of the lung shunt fraction, dedicated liver and lung VOIs were created using the activity map of the XCAT phantom. The liver VOI was equal to all liver voxels of the phantom and the lung VOI was equal to all lung voxels of the phantom. Both VOIs were dilated by 1 cm to include voxels affected by collimator blurring and partial volume effects. Voxels present in both the lung VOI and the liver VOI were attributed to the liver VOI.

To achieve an accurate lesion delineation which can be used to calculate dose distributions in radioembolization, small accumulations of activity in regions with background activity should be detectable. Visibility of the lesion was therefore quantified with the contrast-to-noise ratio (CNR) as:

$$CNR = \frac{C_l - C_b}{\sigma_b}, \quad (2)$$

where C_l is the mean activity concentration in the lesion VOI, C_b is the mean activity concentration in the background VOI, and σ_b is the standard deviation of the activity concentration in the background VOI. According to the Rose criterion, a lesion can be reliably distinguished from the background if the CNR is larger than 5.[24]

Quantitative reconstruction accuracy was assessed by calculating the ARC as:

$$ARC = \frac{A_{VOI}}{A_{GT}} \cdot 100\%, \quad (3)$$

where A_{VOI} is the total activity in the reconstructed VOI (liver or lesion) and A_{GT} is the ground truth total activity as simulated in the phantom.

When dose planning is based on the partition model, T/N ratio is used in the estimation of the expected tumor and healthy liver dose, given the distribution of ^{99m}Tc-MAA in the liver and the lungs.[25] T/N ratio was calculated as:

$$T/N = \frac{\bar{A}_l}{\bar{A}_b}, \quad (4)$$

where $\bar{A}_l$ is the mean activity concentration in the lesion VOI and $\bar{A}_b$ is the mean activity concentration in the background VOI. In the partition model, this ratio is subsequently used to calculate the activity to be administered as follows:[26]

$$A_{adm} = \frac{D_{liver}(T/N \cdot M_{lesion} + M_{liver})}{D_{abs}(1 - \frac{LSF}{100})}, \quad (5)$$

where A_{adm} is the activity [GBq] to be administered, D_{liver} is the maximum allowed dose to the liver tissue [Gy], T/N is the tumor/non-tumor ratio, M_{lesion} is the mass of the lesion [kg], M_{liver} is the mass of the liver [kg], D_{abs} is the assumed absorbed dose per GBq per kilogram tissue (50 J/GBq), and LSF is the lung shunt fraction [%].

Lung shunt fraction is defined as the percent of the administered activity shunting to the lungs and is important for estimating the dose on the lungs, which limits the therapeutic activity given to the patient.[27] LSF was calculated as:

$$LSF = \frac{A_{lung}}{A_{lung} + A_{liver}} \cdot 100\%, \quad (6)$$

where A_{lung} is the total activity in the lung VOI and A_{liver} is the total activity in the liver VOI. Note that a different set of VOIs is used in the LSF calculation than in the calculation of the other image quality metrics.

2.D. Phantom experiment

To further verify the effect of shortening the total acquisition time on image quality and dosimetry, experimental SPECT/CT acquisitions of an anthropomorphic phantom (Model ECT/TOR/P) were performed. A sphere of 20 mm diameter was positioned inside the liver and was filled with 3 MBq of ^{99m}Tc. The rest of the liver compartment was filled with 140 MBq of ^{99m}Tc, resulting in a T/N ratio of 7.6:1. In addition, the lungs contained 10 MBq of ^{99m}Tc, giving an LSF of 6.7%.

SPECT/CT scans were performed on a Symbia T SPECT/CT system (Siemens Healthcare, Erlangen, Germany) with a LEHR collimator. Scans with a uniform projection-time protocol with total acquisition times of 1, 2, 5, 10, and 30 min, respectively, were acquired. In addition, scans of 0.5 and 2.5 min were acquired to simulate uniform projection-time protocol single-head acquisitions of 1 and 5 min, respectively. Projections were acquired at 120 angles (60 views) on a matrix of 128 × 128 pixels, a zoom factor of 1 and with the energy window positioned at 140 keV ± 7.5% and a lower scatter window at 118 keV ± 7.5%.

All acquired projection sets were reconstructed with the clinical reconstruction protocol (3DOSEM, 6 iterations, 8 subsets, attenuation correction, dual-window scatter correction, 5.0 mm Gauss filter) and with UMCS, using the same reconstruction parameters as described in Section 2.B.2 (attenuation correction, Monte Carlo scatter correction), to investigate the effect of reconstruction software on image quality and dosimetry metrics. In conformity with the clinical reconstructions, the UMCS reconstructions used six iterations and were smoothed with a 5.0 mm Gauss filter.

VOIs were manually delineated on the low-dose CT images, after which masks for lesion, background, lungs, and liver were generated in the same fashion as for the digital phantom. Subsequently, CNR, ARC, T/N ratio, and LSF were calculated for each combination of scan duration and reconstruction method. Because the clinical reconstruction protocol resulted in voxel values representing counts instead of Bq/voxel, the ARC for these reconstructions were calculated relative to the clinical reconstruction of the 30 min SPECT scan.

2.E. Statistical analysis

The calculated image quality metrics were compared against the corresponding reference value (bold in Table II) to investigate whether the change in a certain parameter had a significant effect on the evaluation of the pretreatment scan. For example, the difference in CNR for the uniform protocol (reference) and the HCS protocol was calculated for all of the 3600 combinations of the other parameters. To assess the relevance of the change, Cohen's d was calculated as follows:

$$d = \frac{m_{diff}}{\sigma_{diff}},$$

where m_{diff} is the mean of the differences and σ_{diff} is the standard deviation of the differences.[28] Cohen proposed to assess the values as follows: small effect ($d < 0.20$), medium effect (around 0.50), and large effect ($d > 0.80$).[28] In this study, we considered values of $d < 0.50$ unlikely to have a relevant effect on the evaluation of the pretreatment procedure. Consequently, data were averaged over parameters that did not have a significant effect.

3. RESULTS

3.A. Simulations

3.A.1. Counts in projections

Usage of the HCS protocol resulted in 35% more counts in the projections than with the uniform projection-time protocol ($d = 0.72$). Lesion size ($d = 0.36$) and lesion location ($d < 0.49$ for all locations) did not influence the number of counts in the projections. The NUS I and NUS II protocols resulted in 18% ($d = 0.71$) and 22% ($d = 1.29$) more counts than the uniform projection-time protocol, respectively (Fig. 3). Similar ratios were found for the other simulated total acquisition times.

3.A.2. Reconstructions

Reconstructed images of the uniform projection-time protocol and the NUS II protocol obtained with a single-head

scanner and the phantom with a 20-mm lesion in segment VII are shown in Fig. 4. For comparison purposes, a reconstructed image of the simulation of the current clinical protocol (uniform, 30 min, dual-head) is also shown. As expected, visibility of the lesion and overall image quality deteriorated with shorter acquisition times.

3.A.3. Contrast-to-noise ratio

Although the use of the nonuniform protocols increased CNR slightly, the effect was considered small (HCS: $d = 0.27, m_{\text{diff}} = 0.45$; NUS I: $d = 0.36, m_{\text{diff}} = 0.50$; NUS II: $d = 0.15, m_{\text{diff}} = 0.20$). CNR decreased significantly with decreasing acquisition times ($2.24 < d < 2.47$) and was lower for the 10-mm lesion than for the 20-mm lesion ($d = 2.00, m_{\text{diff}} = -10.59$) [Fig. 5(a)]. The lowest CNR was found consistently in segment I ($d = 1.22, m_{\text{diff}} = -2.47$), while segments II and III showed the highest CNR (II: $d = 0.64, m_{\text{diff}} = 1.06$; III: $d = 0.74, m_{\text{diff}} = 1.23$).

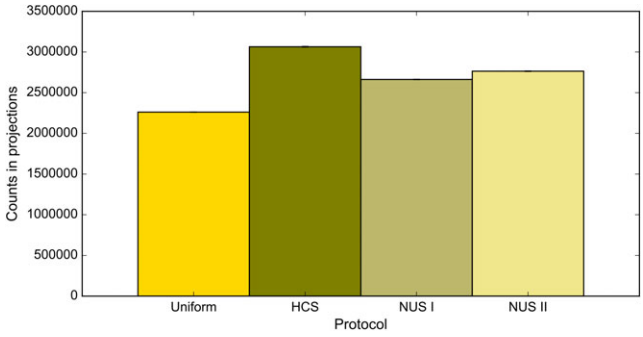

FIG. 3. Number of counts in projections obtained with the different protocols for a single-head geometry with a total acquisition time of 10 min, averaged over all lesion positions and sizes. Error bars (too small to be visible) indicate standard deviations. [Color figure can be viewed at wileyonlinelibrary.com]

According to the Rose criterion (CNR > 5), the 20-mm lesion was distinguishable from the background in all liver segments for scans of 1 min and longer, both with a dual- and a single-head system. The 10-mm lesion reached a CNR larger than 5 in all liver segments with a dual-head scan of 5 min and longer, while a single-head scan had to take at least 10 min.

Since CNR is a combination of contrast and noise, more insight into the effect of nonuniform projection-time protocols can be obtained by looking at these components separately. A more pronounced advantage of the nonuniform projection-time protocols was seen when only the noise in the background VOI [σ_b in Eq. (2)] was taken into account, showing a substantial reduction in the background noise (HCS: $d = 1.28, m_{\text{diff}} = -247.36$; NUS I: $d = 0.86, m_{\text{diff}} = -97.21$; NUS II: $d = 0.59, m_{\text{diff}} = -72.82$) [Fig. 5(b)]. Lesion size and lesion location did not have an effect on the noise level ($d < 0.27$). Contrast, however, was lower when nonuniform protocols were used compared to the uniform protocol, diminishing the advantage of nonuniform projection-time protocols with respect to CNR.

3.A.4. Activity recovery coefficient

Ideally, an ARC of 100% would be obtained, meaning that all activity in the phantom is quantitatively correctly reconstructed. Activity recovery in the background VOI showed a consistent minor overestimation of 2 percentage points (pp) for all lesion sizes, lesion positions, acquisition times, and acquisition protocols. Activity recovery in the lesion was lower for the 10-mm lesion than for the 20-mm lesion ($d = 3.05, m_{\text{diff}} = -24.85$ pp) (Fig. 6). Shortening acquisition time did not influence mean activity recovery, although it increased the standard deviation ($0.00 < d < 0.09$). The lowest activity recovery was found

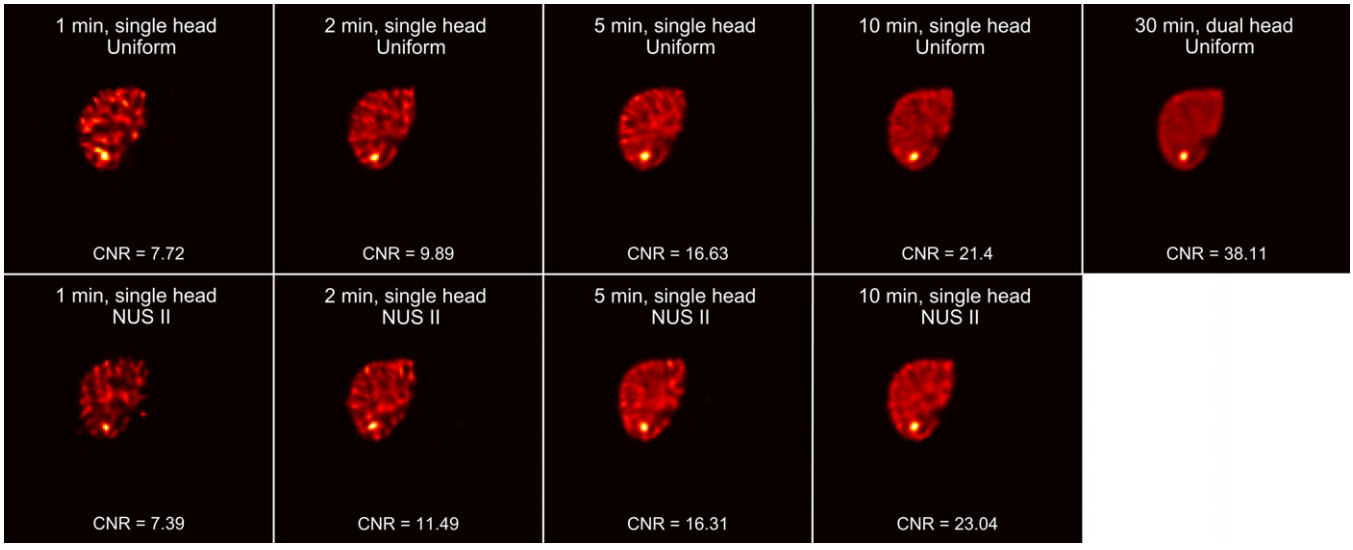

FIG. 4. Reconstructed images of the uniform (upper row) and NUS II (lower row) protocol obtained with a single-head scanner and the phantom with a 20 mm lesion in segment VII. For comparison purposes, a reconstructed image of the simulation of the current clinical protocol (uniform, dual-head, 30 min) is also shown. [Color figure can be viewed at wileyonlinelibrary.com]

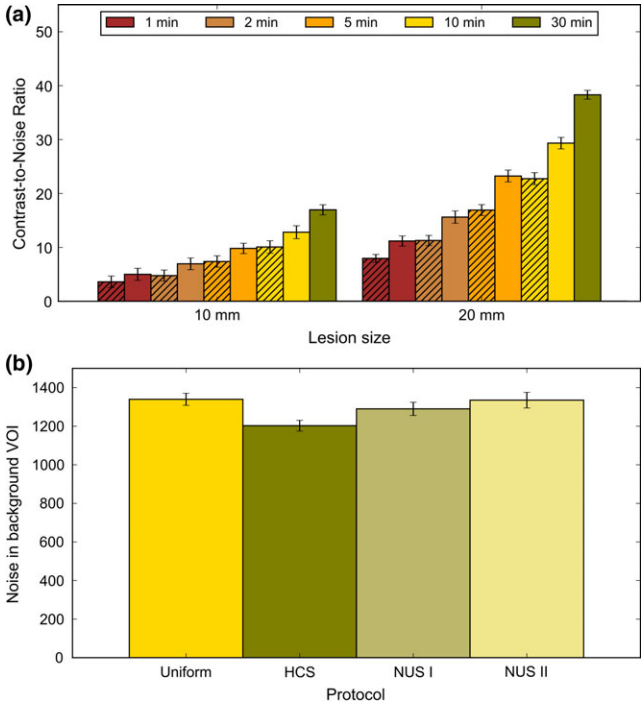

FIG. 5. (a) CNR values for different acquisition times for the lesion in segment VIII (reference), averaged over all protocols. Cross-hatched and solid bars correspond to the single-head and the dual-head data, respectively. (b) Noise levels for the different protocols for a single-head geometry with a total acquisition time of 10 min, averaged over all lesion positions and sizes. Error bars indicate standard deviations. [Color figure can be viewed at wileyonlinelibrary.com]

for the lesion in segment I ($d = 1.18, m_{\text{diff}} = -10.56$ pp) and the highest activity recovery was achieved for lesions in segment II or III (II: $d = 0.56, m_{\text{diff}} = 4.45$ pp; III: $d = 0.57, m_{\text{diff}} = 4.40$ pp). Usage of nonuniform projection-time protocols did not improve activity recovery coefficients. On the contrary, the HCS protocol decreased ARC slightly for almost all lesion positions ($d = 0.27, m_{\text{diff}} = -3.24$ pp), while usage of the NUS I or NUS II protocol led to similar ARC values as the uniform projection-time protocol (NUS I: $d = 0.01, m_{\text{diff}} = 0.05$ pp; NUS II: $d = 0.00, m_{\text{diff}} = -0.00$ pp).

3.A.5. T/N ratio

For all lesion sizes, positions, and acquisition times, the T/N ratio was lower than in the ground truth (8:1) due to partial volume effects and incomplete activity recovery. The same trends as for activity recovery were seen, with lower T/N ratios for the 10-mm lesion than for the 20-mm lesion in all segments ($d = 5.65, m_{\text{diff}} = -2.04$) and a reduced T/N ratio in segment I compared to segment VIII ($d = 1.23, m_{\text{diff}} = -0.48$) (Fig. 7). Similarly, usage of nonuniform projection-time protocols did not improve T/N ratio (HCS: $d = 0.46, m_{\text{diff}} = -0.12$; NUS I: $d = 0.01$, $m_{\text{diff}} = 0.00$; NUS II: $d = 0.02, m_{\text{diff}} = -0.01$). The T/N ratio decreased slightly with the HCS protocol. This is linked to the lower ARC in the HCS protocol.

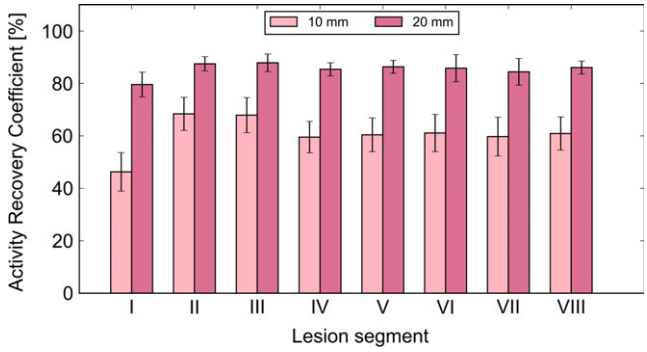

FIG. 6. ARC values for the 10 and 20 mm lesion in segment I–VIII, averaged over all protocols and acquisition times. Ideally, a value of 100% would be obtained. Error bars indicate standard deviations. [Color figure can be viewed at wileyonlinelibrary.com]

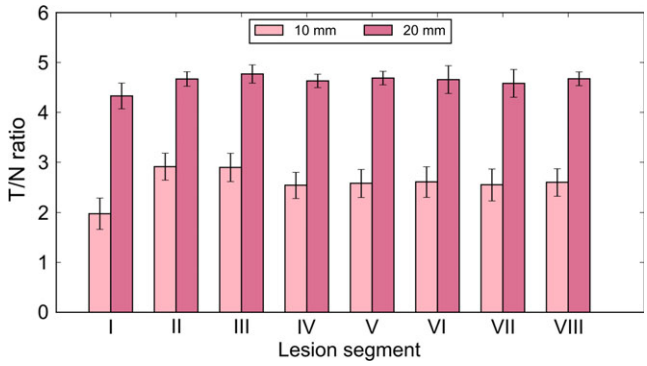

FIG. 7. T/N ratios for the 10 and 20 mm lesion in segments I–VIII, averaged over all protocols and acquisition times. Ideally, a T/N ratio of 8 would be obtained. Error bars indicate standard deviations. [Color figure can be viewed at wileyonlinelibrary.com]

3.A.6. Lung shunt fraction

No influence of lesion size or location was seen in the estimated lung shunt fraction ($d < 0.08$). Shortening acquisition times did have an effect on the LSF estimations ($0.51 < d < 1.17$), but the mean differences were small and unlikely to affect clinical decisions ($m_{\text{diff}} < 0.12$ pp) [Fig. 8(a)]. The HCS protocol resulted in lower LSF estimates ($d = 1.21, m_{\text{diff}} = -0.11$ pp) compared to the uniform projection-time protocol, the other nonuniform projection-time protocols did not influence LSF estimates (NUS I: $d = 0.07, m_{\text{diff}} = -0.01$ pp; NUS II: $d = 0.30$, $m_{\text{diff}} = -0.04$ pp) [Fig. 8(b)]. In all cases, LSF was estimated accurately, with a difference of less than 0.5 pp with the ground truth of 5%.

3.B. Phantom experiment

Image quality measured with the physical phantom showed similar behavior in relation to acquisition times as our simulations. In general, the results of image reconstructions of the physical phantom were comparable to those of the Monte Carlo simulations.

The clinical reconstruction method resulted in slightly lower CNR values than the Monte Carlo reconstructions

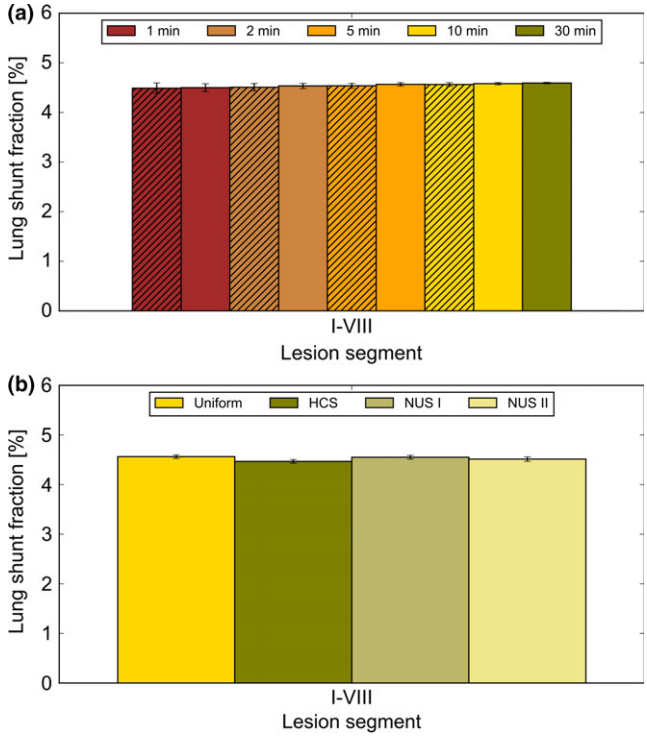

FIG. 8. (a) Estimated LSF averaged over all lesion positions and sizes for different acquisition times. Cross-hatched and solid bars correspond to the single-head and the dual-head data, respectively. (b) Estimated LSF obtained from the different a single-head scanner and a total acquisition time of 10 min, averaged over all lesion positions and sizes. A lung shunt fraction of 5% was simulated in the phantom. Error bars indicate standard deviations. [Color figure can be viewed at wileyonlinelibrary.com]

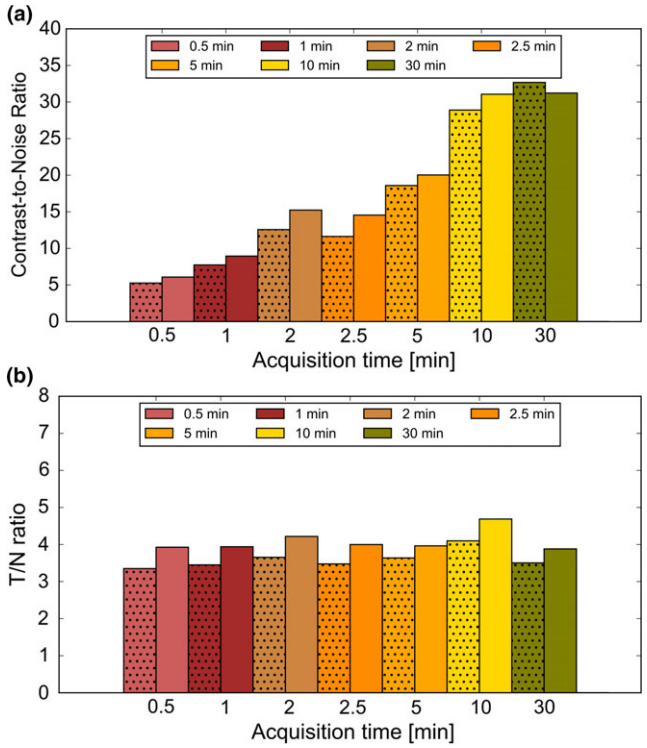

FIG. 9. Comparison between clinical and Monte Carlo reconstructions of the phantom experiment: (a) CNR values and (b) T/N ratios. Ideally, a T/N ratio of 7.6 would be obtained. Speckled and solid bars correspond to clinical and Monte Carlo data, respectively. [Color figure can be viewed at wileyonlinelibrary.com]

[Fig. 9(a)]. Activity recovery in the background VOI showed an overestimation of approximately 4 pp for all acquisition times. Activity recovery in the lesion was stable at approximately 56% for all acquisition times (data not shown). In the clinical reconstructions, activity recovery was stable with respect to the reconstruction of the 30-min scan in both the background and the lesion. For the Monte Carlo reconstructions, T/N ratios were comparable to the digital phantom [Fig. 9(b)]. However, clinical reconstructions resulted in slightly lower T/N ratios than the Monte Carlo reconstructions. LSF was stably estimated at approximately 6%, with a maximum deviation of 1 pp compared with the ground truth of 6.7%, regardless of the reconstruction method and acquisition time.

4. DISCUSSION

Fast and accurate dosimetry in the interventional suite has the potential of shortening treatment times and improving treatment accuracy. The aim of this study was to investigate the feasibility of acquiring fast liver SPECT scans without compromising the evaluation of the pretreatment procedure for radioembolization dosimetry and treatment planning. In addition, the potential benefit of three nonuniform acquisition projection-time protocols was evaluated. The results of the simulations were verified with a phantom experiment.

Fast quantitative liver SPECT images should be of sufficient quality to reliably calculate metrics required for treatment planning in radioembolization. In clinical practice, T/N ratio and LSF estimation are the most important metrics as they are used in the partition model.[25] The results show that acquisition times can be as short as 1 min for dosimetric quantities based on whole-organ VOIs (i.e., ARC, T/N ratio, and LSF) when tumor delineations are known from pretreatment CT or magnetic resonance imaging (MRI), while still giving similar results as the current clinical practice. This is in accordance with the findings presented by Vanhove et al.[29], where the effect of shortened acquisition time on whole-organ dosimetry after administration of indium-111 was investigated. As expected, shortening acquisition times reduced image quality in terms of CNR. Acquisition times of at least 10 min were needed to reliably distinguish the simulated lesions from the background. CNR is, however, of minor importance for assessment of the ^{99m}Tc-MAA activity during radioembolization.

We did not find any benefit from using nonuniform projection-time acquisition protocols. The HCS protocol was based on clinically used dedicated cardiac scanners, where scanning 180 degree is common clinical practice. The HCS protocol resulted in 35% more counts than obtained with the uniform protocol. However, those extra counts did not translate directly into better image quality. Although noise levels decreased markedly, CNR values, T/N ratios, and

activity recovery coefficients did not change significantly. Theoretically, a 180-degree acquisition should be sufficient for reconstruction when the system matrix is exactly known. However, due to attenuation, and to a lesser extent due to scatter, depth-dependent collimator-detector response and noise, projections from a 180-degree acquisition hold less information than projections of a 360-degree acquisition. This results in less accurate reconstructions with the HCS protocol. In addition, reconstructions of projections from a 180-degree acquisition converge more slowly and to lower activity concentration values than reconstructions of a 360-degree acquisition. In cardiac imaging, it was shown that a 180-degree arc was related to inhomogeneities and quantitation errors.[30–32] This is in line with our results, showing no significant difference in image quality and dosimetric accuracy in images obtained with the HCS protocol compared with images obtained with the uniform projection-time protocol. The NUS I and II protocols were based on results found in literature.[14–17] Similarly as for the HCS protocol, the number of counts increased, but this did not result in better image quality.

Several studies in the literature showed improvement in CNR values upon usage of nonuniform projection-time protocols.[14–17] In these studies, the acquisition protocol was optimized to a specific phantom. Although the protocols used in our study were based on these optimal protocols, where more time was spent at angles with a high count rate, our results did not show a substantial increase in CNR values. This could be because the optimized protocols used highly varying acquisition time distributions, while our protocols consisted of at most four different time windows. But more importantly, the largest improvement in image quality was found when quite simplistic phantoms with heavily asymmetrical activity distributions were used. The more realistic phantom of our study had a less asymmetrical activity distribution, potentially lessening the effect of nonuniform acquisition protocols.

The dependence of image quality and dosimetry metrics on acquisition time was not significantly influenced by the position of the lesions, although the lowest CNR, ARC, and T/N ratios were consistently found for lesions in segment I. Segment I, the caudate lobe, is located centrally at the posterior side of the liver. Consequently, counts originating from lesions in this traverse more tissue and thus undergo more attenuation. This resulted in a lower CNR, ARC, and T/N ratio compared with lesions in other segments.

Image quality is a function of reconstruction parameters and the number of counts in the projections. In this study, the effect of the latter is investigated by shortening acquisition times and comparing single- and dual-head systems. With equal total acquisition times, a single-head system results in half the counts of a dual-head system, lowering image quality. The number of counts in the projections is also influenced by the activity administered to the patient. Equivalent image quality can be obtained in half the time when the activity is doubled. However, patient dose considerations limit increasing administered activity, this scenario is therefore not evaluated in this study.

Computation time of a single reconstruction with UMCS on a single-threaded regular desktop computer is about 30 min. This is unacceptably long for inclusion in a 1-day procedure. However, the differences found between the clinical reconstructions of the physical phantom and our Monte Carlo-based UMCS reconstructions were small and unlikely to affect clinical decisions. The results of this paper will therefore also be valid for reconstruction methods using window-based scatter correction methods instead of Monte Carlo-based scatter correction as is used in UMCS. Accordingly, the standard reconstruction protocol, which takes only several minutes, is sufficient to reconstruct the ^{99m}Tc-MAA distribution in radioembolization procedures. Monte Carlo-based scatter correction might, however, be needed when posttreatment scans with other isotopes having more complex emission spectra, such as holmium-166 or yttrium-90, are evaluated.

The number of iterations used in iterative reconstruction is a trade-off between quantification and noise amplification.[33] In our simulations, we were primarily interested in quantification, leading to the choice of using 10 iterations. In clinical practice, however, quantification is often less critical than noise amplification; reconstructions are therefore stopped after fewer (e.g., 6) iterations. This number of iterations was also used in our physical phantom experiment to verify the results with standard clinical protocols.

We did not incorporate breathing motion into our analysis in order to solely study the effects of shortening acquisition times and using nonuniform projection-time protocols. It is expected that breathing motion will deteriorate dosimetric accuracy.[34] However, the amount of deterioration due to breathing motion is expected to be independent of total acquisition time.

To limit the number of varied parameters in this study, LSF and T/N ratio were fixed. We expect LSF to be stably estimated at short acquisition times.[12] Due to the large ROIs used in LSF estimation, the impact of increased noise is negligible when shortening acquisition times. Limited research on the effect of a lower T/N ratio showed that similar behavior with respect to acquisition time and protocol can be expected.

We further acknowledge the limitation of a simulation study being of restricted realism. In clinical practice, wide variations in lesion size, position and body type will be seen. By simulating two rather small lesions at different positions in the liver, we sought to recapitulate part of the clinical variation in this study. In addition, a simulation study has the benefit of having a ground truth to which results can be compared and the possibility of simulating many acquisition times. In a clinical study, such an extensive search for possible protocols and acquisition times will not be possible.

This study focused specifically on accelerating nuclear imaging at the interventional suite for liver radioembolization procedures. Nevertheless, the results are equally valid for shortening acquisition times of scans generally. Specifically, scans for other purposes than radioembolization using similar metrics derived from large ROIs, thus cancelling the noise

increase related to shortening acquisition times, could potentially be executed in shorter times than in current clinical practice.

5. CONCLUSION

The effect of shortening acquisition times for fast quantitative liver SPECT on image quality and dosimetric accuracy was investigated, and simulations were verified with a phantom experiment. The results showed that shortening acquisition times decreased CNR, which could be slightly counteracted by using nonuniform projection-time protocols. Dosimetric accuracy was not affected by shortening acquisition times. Usage of a nonuniform projection-time protocol did not improve dosimetric accuracy. Therefore, acquisition times can be safely lowered to 10 min with a uniform projection-time protocol for the assessment of the pretreatment procedure in the interventional suite, solving one of the major issues related to 1-day procedures in radioembolization.

ACKNOWLEDGMENTS

This work is part of the research program Innovational Research Incentives with project number 12977 which is (partly) financed by the Netherlands Organisation for Scientific Research (NWO).

CONFLICTS OF INTEREST

The authors declare no conflicts of interest.

[a]Author to whom correspondence should be addressed. Electronic mail: s.vandervelden-3@umcutrecht.nl; Telephone: +31887567571; Fax: +31887555491.

REFERENCES

1. Braat AJAT, Smits MLJ, Braat MNGJA, et al. ^{90}Y hepatic radioembolization: an update on current practice and recent developments. *J Nucl Med*. 2015;56:1079–1087.
2. Kennedy A, Coldwell D, Sangro B, Wasan H, Salem R. Radioembolization for the treatment of liver tumors. *Am J Clin Oncol*. 2012;35:91–99.
3. Smits MLJ, Elschot M, Sze DY, et al. Radioembolization dosimetry: the road ahead. *Cardiovasc Intervent Radiol*. 2015;38:261–269.
4. Kao YH, Hock Tan AE, Burgmans MC, et al. Image-guided personalized predictive dosimetry by artery-specific SPECT/CT partition modeling for safe and effective ^{90}Y radioembolization. *J Nucl Med*. 2012;53:559–566.
5. Gates VL, Marshall KG, Salzig K, Williams M, Lewandowski RJ, Salem R. Outpatient single-session yttrium-90 Glass microsphere radioembolization. *J Vasc Interv Radiol*. 2014;25:266–270.
6. Gabr A, Kallini JR, Gates VL, et al. Same-day ^{90}Y radioembolization: implementing a new treatment paradigm. *Eur J Nucl Med Mol Imaging*. 2016;43:2353–2359.
7. Garin E, Edeline J, Rolland Y. High impact of preferential flow on ^{99m}Tc-MAA and ^{90}Y-loaded microsphere uptake correlation. *J Nucl Med*. 2016;57:1829–1830.
8. Gardiazabal J, Esposito M, Matthies P, et al. Towards personalized interventional SPECT-CT imaging. In: Golland P, Hata N, Barillot C, Hornegger J, Howe R, eds. *Medical Image Computing and Computer-Assisted Intervention – MICCAI 2014*. Lecture Notes in Computer Science (Including Subseries Lecture Notes in Artificial Intelligence and Lecture Notes in Bioinformatics). Vol. 8673; Cham: Springer; 2014:504–511.
9. Engelen T, Winkel BM, Rietbergen DD, et al. The next evolution in radioguided surgery: breast cancer related sentinel node localization using a freehand SPECT-mobile gamma camera combination. *Am J Nucl Med Mol Imaging*. 2015;5:233–245.
10. Beijst C, Elschot M, Viergever MA, de Jong HWAM. Toward simultaneous real-time fluoroscopic and nuclear imaging in the intervention room. *Radiology*. 2016;278:232–238.
11. van der Velden S, Beijst C, Viergever MA, de Jong HWAM. Simultaneous fluoroscopic and nuclear imaging: impact of collimator choice on nuclear image quality. *Med Phys*. 2017;44:249–261.
12. van der Velden S, Bastiaannet R, Braat AJAT, Lam MGEH, Viergever MA, de Jong HWAM. Estimation of lung shunt fraction from simultaneous fluoroscopic and nuclear images. *Phys Med Biol*. 2017;62:8210–8225.
13. Elschot M, Nijsen JFW, Lam MGEH, et al. ^{99m}Tc-MAA overestimates the absorbed dose to the lungs in radioembolization: a quantitative evaluation in patients treated with ^{166}Ho-microspheres. *Eur J Nucl Med Mol Imaging*. 2014;41:1965–1975.
14. Fuin N, Pedemonte S, Arridge S, Ourselin S, Hutton BF. Use of the Fisher Information Matrix to optimize the acquisition protocol for a D-SPECT system. In: 2012 IEEE Nuclear Science Symposium and Medical Imaging Conference Record (NSS/MIC). IEEE; 2012:2137–2142.
15. Pato LRV, Vandenberghe S, Van Holen R. Efficient optimization for adaptive SPECT systems based on local shift-invariance. In: 2012 IEEE Nuclear Science Symposium and Medical Imaging Conference Record (NSS/MIC). IEEE; 2012:2501-2508.
16. Cai L, Li N, Meng LJ. A prototype adaptive SPECT system with self-optimized angular sampling. In: 2011 IEEE Nuclear Science Symposium Conference Record. IEEE; 2011:4402-4406.
17. Zheng X, Metzler SD. Angular viewing time optimization for slit-slat SPECT. In: 2012 IEEE Nuclear Science Symposium and Medical Imaging Conference Record (NSS/MIC). IEEE; 2012:3521-3524.
18. Segars WP, Sturgeon G, Mendonca S, Grimes J, Tsui BMW. 4D XCAT phantom for multimodality imaging research. *Med Phys*. 2010;37:4902–4915.
19. Willowson KP, Tapner M, Bailey DL. A multicentre comparison of quantitative ^{90}Y PET/CT for dosimetric purposes after radioembolization with resin microspheres. *Eur J Nucl Med Mol Imaging*. 2015;42:1202–1222.
20. Beekman FJ, De Jong HWAM, Van Geloven S. Efficient fully 3-D iterative SPECT reconstruction with Monte Carlo-based scatter compensation. *IEEE Trans Med Imaging*. 2002;21:867–877.
21. de Jong HWAM, Slijpen ETP, Beekman FJ. Acceleration of Monte Carlo SPECT simulation using convolution-based forced detection. *IEEE Trans Nucl Sci*. 2001;48:58–64.
22. Hendricks JS, Mckinney GW, Waters LS, et al. MCNPX Extensions version 2.5.0; 2005 (April 2005):83.
23. Siemens Healthineers. *Symbia S and T System Specifications*; 2010.
24. Rose A. The sensitivity performance of the human eye on an absolute scale. *J Opt Soc Am*. 1948;38:196.
25. Ho S, Lau WY, Leung TWT, et al. Partition model for estimating radiation doses from yttrium-90 microspheres in treating hepatic tumours. *Eur J Nucl Med*. 1996;23:947–952.
26. Sirtex Medical Limited. *SIR-Spheres® Microspheres - Training Program*. North Sydney, NSW, Australia; 2004.
27. Sirtex Medical Limited. *SIR-Spheres Package Insert (CR1507)*. North Sydney, NSW, Australia; 2012.
28. Cohen J. Statistical power analysis for the behavioral sciences. *Biometrics*. 1970;26:588.
29. He B, Frey EC. Effects of shortened acquisition time on accuracy and precision of quantitative estimates of organ activity. *Med Phys*. 2010;37:1807–1815.
30. Vanhove C, Franken PR, Defrise M, Bossuyt A. Comparison of 180° and 360° data acquisition for determination of left ventricular function from gated myocardial perfusion tomography and gated

blood pool tomography. *Eur J Nucl Med Mol Imaging*. 2003;30:1498–1504.
31. Liu Y, Lam PT, Sinusas AJ, Wackers FJT. Differential effect of 180° and 360° acquisition orbits on the accuracy of SPECT Imaging: quantitative evaluation in phantoms. *J Nucl Med*. 2002;43:1115–1125.
32. Misaka T, Hosono M, Kudo T, et al. Influence of acquisition orbit on phase analysis of gated single photon emission computed tomography myocardial perfusion imaging for assessment of left ventricular mechanical dyssynchrony. *Ann Nucl Med*. 2017;31:235–244.
33. Hudson HM, Larkin RS. Accelerated image reconstruction using ordered subsets of projection data. *IEEE Trans Med Imaging*. 1994;13:601–609.
34. Bastiaannet R, Viergever MA, de Jong HWAM. Impact of respiratory motion and acquisition settings on SPECT liver dosimetry for radioembolization. *Med Phys*. 2017;44:5270–5279.